Article

Phase Change Cooling of a Metal Hydride Reactor for Rapid Hydrogen Absorption

Matthew Duncan Keith, Vamsi Krishna Kukkapalli and Sunwoo Kim *

Mechanical Engineering Department, University of Alaska Fairbanks, Fairbanks, AK 99775, USA;
matthewduncankeith@gmail.com (M.D.K.); vkukkappalli@alaska.edu (V.K.K.)
* Correspondence: swkim@alaska.edu; Tel.: +1-907-474-6096

Abstract: As the world is keen on cleaner and sustainable energy, hydrogen energy has the potential to be part of the green energy transition to replace fossil fuels and mitigate climate change. However, hydrogen energy storage is a difficult task since physical storage in the form of compressed gas under high pressure is associated with safety issues. Another form of hydrogen storage is material-based storage, which is the safest way to store hydrogen energy in a particulate matter, known as metal hydrides. Metal hydrides can store hydrogen at room temperature and use less volume to store the same amount of hydrogen compared to classical gas tanks. The challenges with the metal hydrides reactor are their slow charging process and the requirement of proper thermal management during the charging process. In this study, a metal hydride reactor model is developed in COMSOL Multiphysics, and the associated heat transfer simulations are performed. The main objective of this research is to optimize the cooling channel design in the metal hydride reactor, where the R-134a coolant rejects heat through both latent and sensible heat transfer. The study showed that the phase-changing coolant and varying convection coefficient along the length of tubes significantly reduce the hydrogen charging time and the peak temperature of the reactor during hydrogen absorption. The pumping power analysis for the R-134a flow was also conducted. The computation results reveal that coolant channel configurations with nine or more tube-passes require significantly large pumping power.

Keywords: metal hydride; energy storage; phase changing cooling; optimization; cooling channels

1. Introduction

Metal hydrides store hydrogen by chemically bonding it to metals and alloys. Metal hydrides offer various advantages over conventional hydrogen storage cylinders due to their low storage pressure and reasonable volumetric storage efficiencies [1–3]. However, one of the major challenges of metal hydride reactors is their slow charging process; currently, various methods are being studied and applied to decrease the charging time [4]. Some studies reduced the charging time emphasis by installing heat exchangers composed of various geometries with additional optimization studies on fin shape or coolant channel tubes [5–12]. Muthukumar et al. developed a 2-D mathematical model and conducted performance analysis of a metal hydride reactor with embedded cooling tubes and optimized the number of tubes throughout the reactor [5]. Nyamsi et al. conducted 2-D numerical simulations aimed to optimize the volume and spacing of the fins on a finned tube heat exchanger; they further studied the effect of the cooling tube diameter and found that the reaction time decreases with an increase in the cooling tube diameter [6]. Nam et al. developed a 3-D hydrogen absorption model and performed simulations of metal hydride system to charge 5 kg of hydrogen in 5 min with multiple heat exchangers along the length of the reactor; they used finned plates, connected via two tubes with heat exchanger fluid [8]. Garrison et al. simulated a single tube heat exchanger with both annular and longitudinal fins; they studied multiple cooling tube diameters, thickness and cooling fin lengths, and concluded that the longitudinal fins were marginally better than the angular fins, and smaller tubes with less spacing lowered the charging time [7]. Bhouri et al.

developed a 2-D model and performed a numerical study using a longitudinally closed honeycomb structure for the foundation of the reactor; the cells were connected to form a fin-like structure, and the optimization was targeted on the number of tubes and their placement [9]. Tubes were placed within each hexagonal cell, which were used as a heat transfer tube. The study reported improvements in the heat transfer process, and the gravimetric and volumetric capacities. Dhaou et al. conducted experiments to evaluate a coil heat exchanger, and Visaria et al. numerically investigated reactors with a coil heat exchanger configuration [10–12]. Visaria et al. concluded in their computational study that the distance from the metal hydride powder to the tube is crucial and the metal hydride particles closer to tube complete the hydriding reaction faster [11,12]. If the maximum distance between the powder and the cooling tube is reduced, a more even reaction can occur, thus, decreasing the charging time.

The objective of this study is to optimize the cooling channel design in the cylindrical metal hydride reactor, where the coolant (R-134a) absorbs heat through both latent and sensible heat transfer. This study takes into consideration multiple coolant path configurations and directly compares them against one another. The comparison between the different coolant path configurations is based on the ratio of coolant tube volume to the total reactor volume. This volume ratio is maintained at 0.1 (total volume of tubes divided by total volume of reactor). Similarly, for simulations completed in two dimensions, the area ratio is 0.1. Several configurations are simulated using COMSOL Multiphysics and compared in terms of the time to 90% reaction completion [13]. After determining the optimum number of passes through the reactor, a secondary optimization study is performed on the heat transfer fins that are attached to the optimum configuration from the first part of the study. The volume and area ratio of the fins to the total volume of the reactor is maintained at 0.04 (4%). All configurations are balanced against the required pumping work for R-134a during optimization.

2. System Configuration

Many types of metal hydrides are being used for solid-state hydrogen storage research, including intermetallic compounds, complex hydrides (such as alanates), borohydrides, nitrides, chemical hydrides, and magnesium hydrides [14,15]. There is no definitive best hydride for solid-state hydrogen storage. When choosing the material, a balance must be achieved between reaction kinetics, density, cyclability, storage capacity, pressure requirements, price, reactivity to impurities, absorption and desorption temperatures, etc. [16]. While one hydride may have promising reaction kinetics or increased maximum storage capacity, the positive attribute is often accompanied by negative attributes, such as increased weight, poor reversibility or instability with water/air [17].

In this study, $Ti_{1.1}CrMn$ was chosen as the hydride material. The hydriding and thermal properties of $Ti_{1.1}CrMn$ have been well documented by previous research [18–22]. In comparison to the most popular hydrides used in research, $LaNi_5$ and $Ti_{1.1}CrMn$ have comparable hydrogen capacity, better kinetics, and smaller reaction enthalpy [22]. $Ti_{1.1}CrMn$ is a High-Pressure-Metal-Hydride (HPMH) that cycles at higher pressures than $LaNi_5$ to maintain the U.S. Department of Energy (DOE) operating temperature range of -40–$85°C$ for on-board metal hydride hydrogen systems [12]. $Ti_{1.1}CrMn$ also offers a relatively low density of 2200 kg/m^3, which is beneficial for on-board applications [10]. Overall, $Ti_{1.1}CrMn$ is a promising metal hydride material and would benefit from additional research.

Reactor Specifications

An ideal reactor size for modularity and onboard applications should be able to hold 250 g of hydrogen. The number of reactor modules on-board a vehicle was based on the vehicle size, purpose, and range. Based on the weight percentage of hydrogen that $Ti_{1.1}CrMn$ can hold, the choice to end the reaction at an average reacted fraction of 0.9 requires 25.74 kg of $Ti_{1.1}CrMn$, which accounts for a volume of about 9.7 L. A constant coolant tube volume ratio of 0.1 was the physical constraint of the optimization process,

bringing the total volume to 10.8 L. The cylindrical reactor was 15 cm in diameter and 61 cm long, excluding an outer shell or other exterior structures. The reactor can be modelled using a two-dimensional cross-section, perpendicular to the tube path to shorten the computation time. In this study, the cross-section was chosen at the end of the cylinder where the coolant (R-134a) first enters the reactor. Figure 1 illustrates the layout within the reactor for the six-pass heat exchanger. In Figure 1, the first image shows the inlet and exit tubes for the coolant, while the other image shows the opposite end of the reactor. The turns were placed on the outside of the reactor to allow for easier two-dimensional modeling.
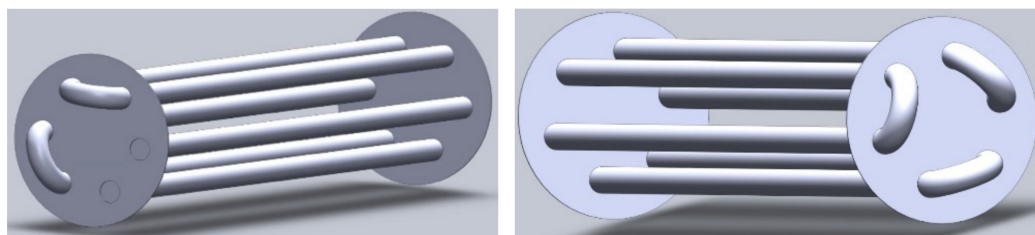

Figure 1. Heat exchanger diagrams.

The constant tube-to-reactor volume ratio implies that all the configurations will hold 250 g of hydrogen at reaction completion. Different simulations were performed by decreasing the diameter of the tubes and concurrently increasing the number of tubes in each scenario to maintain the volume ratio constant. The tubes and fins were modeled as 6061-T6 aluminum with 1 mm thick walls. The configurations that were tested are shown in Figure 2, which include 2-, 3-, 4-, 5-, 6-, 9-, 12-, and 18-pass heat exchangers. The tube-only configurations (unfinned) had the same tube diameters at the same locations as their finned counterparts; the only difference is whether the tubes have fins or not. The tubes were evenly distributed about the center of the reactor with multiple tube spacing diameters tested for each number of passes to find the optimum spacing of the tubes. The next phase of simulations involved adding twelve longitudinal fins per tube accounting for an additional 4% of the total volume, as seen in Figure 2. Figure 3 shows the schematic of the six-pass configuration with labels that explicitly refer to each part. The tubes were numbered in a counterclockwise spiral pattern, beginning with the furthest right tube.
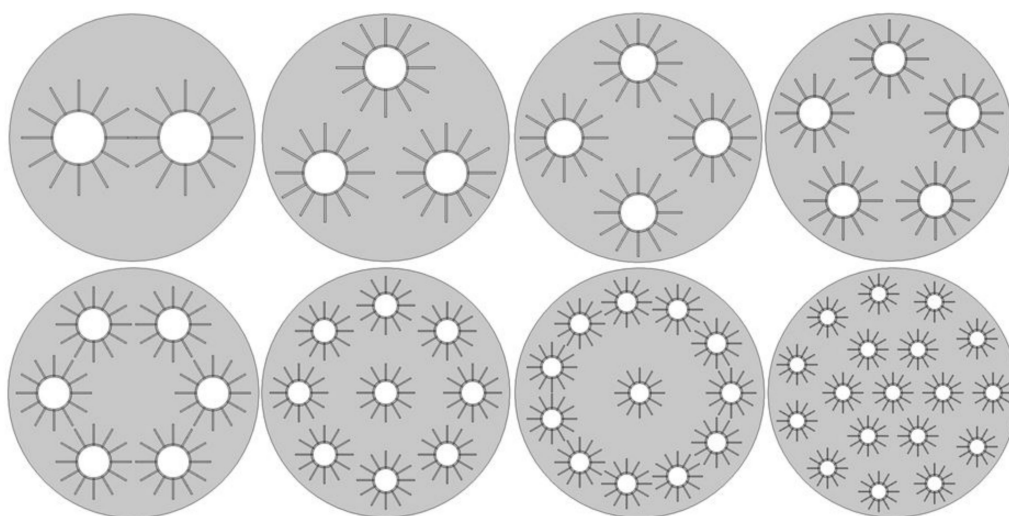

Figure 2. Cross-sectional configurations of the reactors with finned 2-, 3-, 4-, 5-, 6-, 9-, 12-, and 18-pass heat exchangers.
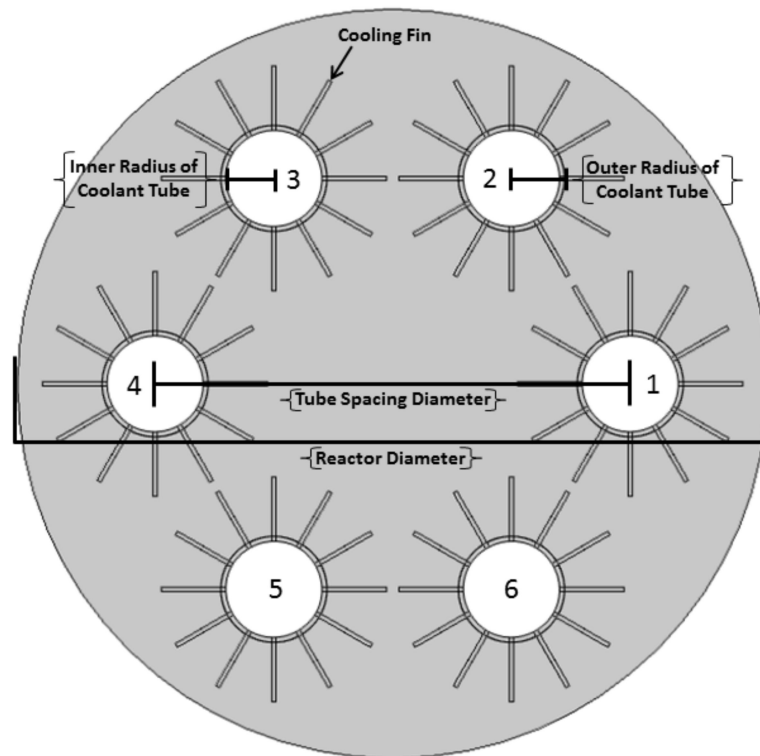
Figure 3. Reactor diagram of a 6-pass finned configuration.

3. Mathematical Modeling

The following assumptions were made for the simulations conducted in COMSOL Multiphysics to reduce the computation time and complexity.

1. The thermal and physical properties of the metal hydride are constant within the operating temperature and pressure range.
2. There is no pressure ramp at the beginning of the simulations. Pressure is instantaneously brought to 280 bar and remains constant during the reaction to simulate a charging station that has a fixed pressure.
3. Heat transfer occurs only in the heat exchanger within the reactor. There is no convection or radiation at the outer shell of the reactor (it is insulated).
4. Contact resistance between the metal hydride and the heat exchanger fins/tubes is assumed to be negligible since the volume changes associated with cycling are ignored. This study aims to optimize the heat exchanger and does not account for contact resistance because it can be reduced using catalysts, material additions [23].
5. Heat transfer coefficients are assumed to be 4200 W/m^2 K at the entrance and 5000 W/m^2 K at the exit. These values are estimated from experimental heat transfer coefficient studies of R-134a with multiple flow rates and tube diameters [24–28].

The 3-dimensional heat conduction equation accounts for the thermal conductivity throughout the metal hydride, heat generation rate, and specific heat of the bed [11]. The metal hydride powder, which is shaded in grey in Figure 3, is the control volume. The plane of Figure 3 represents the *x* and *y* of the rectangular coordinate with *z* as the third coordinate perpendicular to the plane. Equation (1) was used to calculate the temperature profile within the reactor, including the hydride and heat exchanger.

$$k_{MH}\left(\frac{\partial^2 T}{\partial x^2} + \frac{\partial^2 T}{\partial y^2} + \frac{\partial^2 T}{\partial z^2}\right) + \dot{q}''' = \rho_{MH}c_{p,MH}\frac{\partial T}{\partial t} \tag{1}$$

The heat generation rate shown in Equation (2) relies on the reaction rate. Other parameters in the equation are the reaction enthalpy and the largest term in the center

representing the amount of hydrogen that can react with the metal hydride. Heat generation rate is described by an equation developed by Visaria et al., which ignores the heat generation due to pressurization [20].

$$\dot{q}''' = \frac{dF}{dt}\frac{(wt\%)\rho_{MH}}{MW_{H_2}}\Delta H_r \tag{2}$$

Equation (3) shows the rate of reaction, which depends mostly on the equilibrium pressure and temperature within the hydride bed. As the temperature of the bed increases, the equilibrium pressure increases, thereby decreasing the rate of reaction [20].

$$\frac{dF}{dt} = C_a \exp\left(-\frac{E_a}{RT}\right)\ln\left(\frac{P}{P_{eq}}\right)(1-F) \tag{3}$$

Equilibrium pressure is modelled by the Van't Hoff equation, as shown in Equation (4). It is usually dependent upon the temperature of the bed with P_o representing atmospheric pressure [20].

$$P_{eq} = P_o \exp\left(\frac{\Delta H_r}{RT} - \frac{\Delta S}{R}\right) \tag{4}$$

All the variables are described in the Nomenclature with the thermophysical properties and dimensions, listed in Table 1. Most of the values in Table 1 were adopted from the literature [11,12,18,20,21,29,30], while the rest were set values in this study.

Table 1. Constant properties.

Variable	Value (Units)	Variable	Value (Units)
A_{HE}	0.001767 (m^2)	MW_{H2}	2.0159 (g/mol)
A_{MH}	0.015904 (m^2)	P_o	101.3 (kPa)
C_a	150 (1/s) [20]	P	280 (bar) [10]
$c_{p,MH}$	750 (J/kg K) [11]	R	8.314 (J/mol K)
D	0.15 (m)	wt%	0.013 [21]
E_a	20,700 (J/mol H^2) [29]	ΔH_r	−14,390 (J/mol H$_2$) [21]
k_{MH}	0.75 (W/m K) [11]	ΔS	−91.3 (J/mol H$_2$) [21]
k_{Al}	167 (W/m K)	ρ_{MH}	2200 (kg/m^3) [10]
L	0.61 (m)	V_{HE-R}	0.1
m_{H2}	0.25 (kg)	φ	0.6 [10]

All parts of the system, including the metal hydride bed, tubes, and fins, were initially at room temperature (20 °C). From the initial condition, the system pressure was instantaneously brought to 280 bar. The initial pressure was set at 280 bar, while the initial equilibrium pressure corresponding to 20 °C was determined using Equation (4) as 116.42 bar. The reactor was set to be fully discharged with a zero reacted fraction ($F = 0$). Substituting the initial temperature, equilibrium pressure, and reacted fraction as 20 °C, 116.42 bar, and 0, respectively, the reaction rate at time zero can be calculated as 0.0167 [1/s] from Equation (3). The coolant, R-134a, entered the reactor at 10 °C. As it absorbs heat, its quality increases.

The outer boundary of the reactor was given an insulated condition. The inner surfaces of the tubes were subject to convection heat transfer by the coolant. Equations (5) and (6) were used to assign the heat transfer coefficients for all tube locations of the configurations, including the heat transfer tubes. The subscript '*i*' on the heat transfer variable, *h*, refers to the tube to which the value applies. The tubes were numbered in a counterclockwise spiral direction, beginning with the furthest right tube (refer to Figure 3). Equation (7) was used to transform the values found from Equations (5) and (6) to a configuration simulated without heat transfer tubes. Equation (7) considers the effect of wall thickness, the thermal conductivity of the tube and interior heat transfer coefficients [28]. Combined into a one-

dimensional conduction equation, an effective heat transfer coefficient can be calculated at different locations along the tube depending on the internal heat transfer coefficient.

$$h_i = 4200 + 800\frac{i-1}{n} \, for \, i = 1, 3, 5 \ldots \tag{5}$$

$$h_i = 4200 + 800\frac{i}{n} \, for \, i = 2, 4, 6 \ldots \tag{6}$$

$$\frac{1}{h_{i,eff}} = \frac{r_2}{h_1 r_1} + \frac{r_2 \ln\left(\frac{r_2}{r_1}\right)}{k_{Al}} \tag{7}$$

Instead of performing computationally intensive three-dimensional simulations, two-dimensional simplifications were accepted. The end of the reactor, where the inlet coolant tube was located, was taken as the cross-section to be tested. The cross-section was identical throughout, as seen in Figure 1, with only the convective heat transfer coefficient changing along the length of the tube. To confirm the validity of this assumption, the inlet, the midpoint, and the end cross-sections were simulated for both the tube-only and finned tube configurations. Comparisons of the charging time, reacted fraction vs. time, and average bed temperature vs. time were made to confirm the assumption. The differences in charging time between the cross-sections were less than 0.05 s. Adding fins decreased the available space for metal hydride by 4%, which accounts for a decrease in the stored hydrogen of about 11 g at $F = 0.9$.

4. H$_2$ Adsorption and Heat Transfer Simulations

Using COMSOL Multiphysics, the geometries were modeled, and the simulation conditions were applied as previously discussed. A general heat transfer module, time dependent solver, and geometric multi-grid linear system solver were adopted. To test the independence of the results with respect to mesh size, we simulated several cases increasing the number of elements until the changes in the numerical results were less than 1%. Table 2 details the radii of the tubes for each configuration and the size of fins to be tested for each finned configuration. The radii of the tubes were the same for both types of configurations. The first phase of simulations involved finding the optimum tube spacing diameter for each number of passes using the tube-only configurations. Refer to Figure 2 for a visual of the tube spacing diameter. The tube spacing diameters were optimized using 5 mm increments and the optimum values are reported in Table 2. Notice the column for the 18-pass heat exchanger contains values in parentheses, which represents the diameter of the inner ring of tubes, while the other number represents the outer ring of tubes.

Table 2. Dimension specifications (the units of the radius, diameter, length, and width are mm).

Number of Passes	2	3	4	5	6	9	12	18
Outer Radius of Tube (mm)	16.77	13.69	11.86	10.61	9.68	7.91	6.85	5.59
Tube Spacing Diameter (mm)	65	85	90	95	95	105	110	120 (60)
Fin Length	9.12	17.81	14.73	13.09	12.00	9.59	8.15	6.54
Fin Width	1.63	1.10	1.00	0.90	0.82	0.68	0.60	0.50

Figure 4 shows the temperature distribution of the 6-pass tube reactor configuration without fins (top) and with fins (bottom) for three average reacted fractions with a temperature scale in Kelvin. Geometrically, the 6-pass with fins is superior to the 6-pass without fins configuration because of the reduced volume of the hot spot reduction in the metal hydride reactor. Additionally, the longitudinal fins on the tube aids in reducing the localized hotspot temperatures, thereby decreasing the charge time.
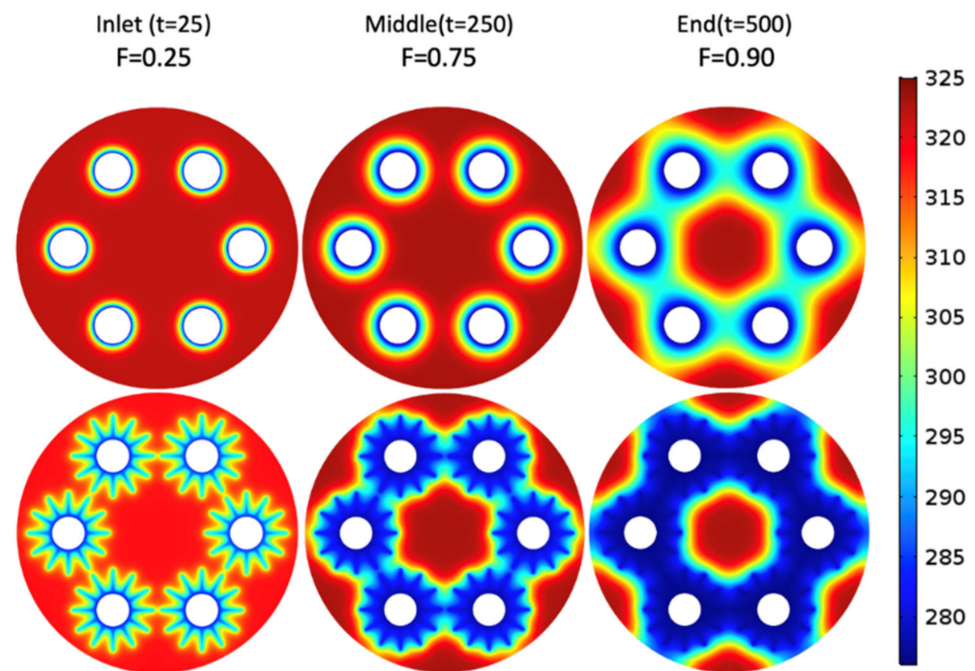
Figure 4. Temperature profiles of the 6-passes tube reactor without fins (**top**) and with fin (**bottom**), Scale in Kelvin.

Figure 5a displays the average reacted fraction for the metal hydride bed throughout the charging process for the tube-only configurations. Initially, the average reacted fraction (*F*) increases rapidly as most of the heat released during the reaction is absorbed as sensible heat. After *F* = 0.3, the profiles diverge due to the differences in heat removal as no more heat can be absorbed as sensible heat. The charging rate declines as the reacted fraction increases because the locations within the reactor closest to the heat exchange tubes first complete the reaction. Metal hydrides have low thermal conductivity, so the heat removal from distant locations within the reactor takes a longer time. Increasing the number of tubes decreases the average distance from the hydride locations to heat exchange tubes, thus decreasing the charging time.
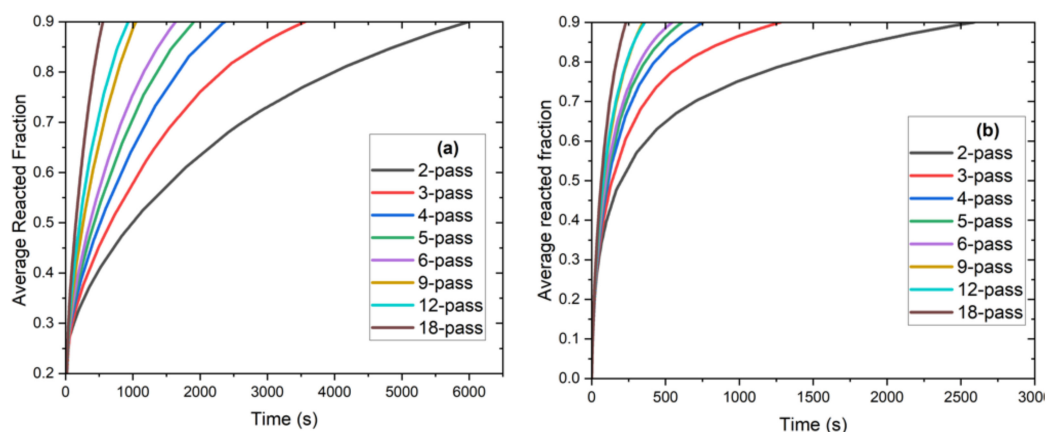

Figure 5. Average reacted fraction vs. time for (**a**) tube-only and (**b**) finned tube configurations.

Twelve fins were added to the optimally spaced tube-only configurations that were discovered from the tube-only simulations. A fin aspect ratio (length divided by width) of roughly 14 was used to find the optimum number of finned tubes for charging. The aspect ratio depends on the available space within the reactor; hence, an aspect ratio of only 5.6 can fit within the two-pass reactor. Figure 5b shows the average reacted fraction over

time for the finned configurations. The main difference between the charging profiles for the tube-only versus finned tube heat exchangers is the slope of the curves. The charging rate is increased due to the decreased average distance to the heat exchange tubes for the finned tube configurations. Further, the charging rate slows at a higher average reacted fraction, which confirms the prediction that the distant locations within the reactor extend the charge time since the locations close to the heat exchanger first complete the reaction. The charging rate is directly correlated to the average bed temperature. Taking the 2-pass as an example from Figure 6, the figure shows the bed temperature cool more slowly beyond 30 °C, which therefore means the charging rate is reduced.
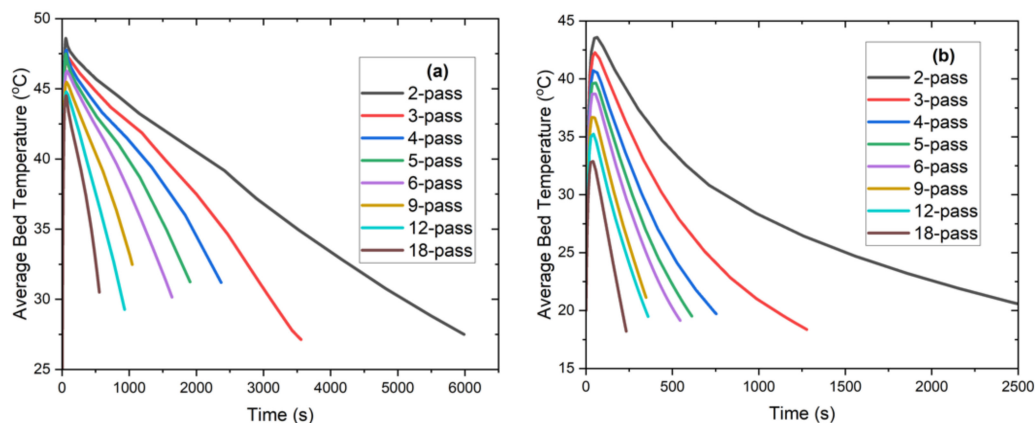

Figure 6. Average bed temperature vs. time till reaction completion for (**a**) tube-only and (**b**) finned tube configurations.

Figure 6a shows the volume-averaged temperature of the metal hydride over time for the tube-only configurations until reaction completion. The final temperatures vary between different reactors because the simulations stop when the reacted fraction F = 0.9. The 2- and 3-pass temperature profiles have relatively lower final temperatures than the other configurations due to the greater maximum distance between some locations of the hydride bed and the fins/tubes than for the models with more tube passes. The locations at the outer rim of the reactor would remain at high temperature with a low reacted fraction, delaying the average reacted fraction from reaching 0.9, while most of the reactor is already at a lower temperature.

The plot in Figure 6b is almost similar to that of Figure 6a, except for the bed temperature, which decreases rapidly at first until the latter part of the charging process. This is the result of a high reaction rate near the heat exchanger, which exists until the nearer locations are charged, while the distant locations remain at a lower reacted fraction. Note that the average temperature at reaction completion is about 10 °C lower for the finned tubes than for the tube-only configurations. This is a form of model validation where the higher rates of reaction are correlated directly with lower temperatures within the metal hydride bed, validated by the equations in Section 3.

From Equation (4), when the equilibrium pressure equals the charging pressure, the system achieves equilibrium, and the charge rate drops to zero. This occurs at about 50 °C, which is validated through simulations as shown in Figure 7. Figure 7 illustrates the maximum temperature within the hydride bed over the charging period. As expected, the maximum temperature remains at about 50 °C for the configurations with larger distances between the heat exchanger and the hydride locations.
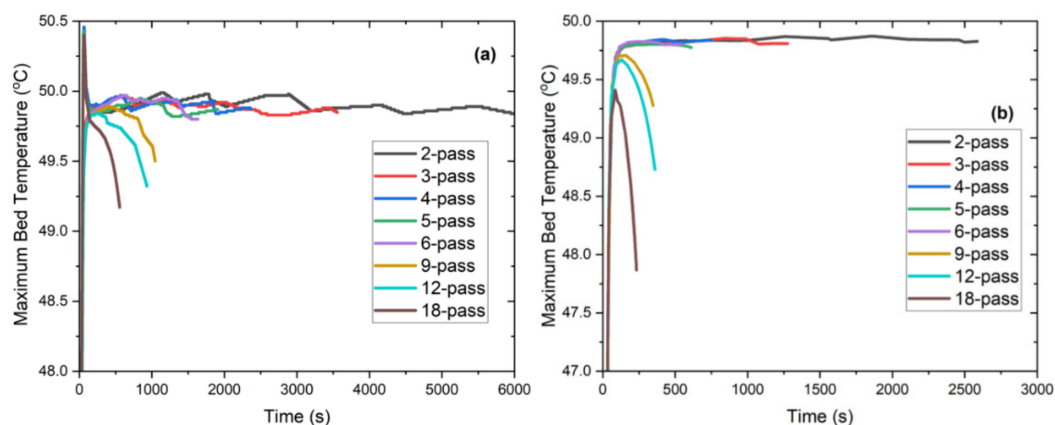
Figure 7. Maximum bed temperature vs. time till reaction completion for (**a**) tube-only and (**b**) finned tube configurations.

The most important parameter during optimization is the time to reaction completion ($F = 0.9$). From Figure 8, it is evident that as the number of passes increases, the charge time decreases rapidly until the 5-pass heat exchanger; a further decrease in the charge time becomes less substantial with additional tubes. The charge time decreases with additional tubes until the effective heat transfer coefficient becomes too small to maintain the trend due to smaller tubes. Based on Equation (7), as the tubes decrease in size, the thermal conductivity (k) of the tube wall material (constant thickness for all tubes) will reduce the effective heat transfer coefficient. Further, more tubes will not yield a sufficient decrease in charge time to warrant the increased cost, manufacturing difficulty, high pumping power, complexity, and decreased durability.
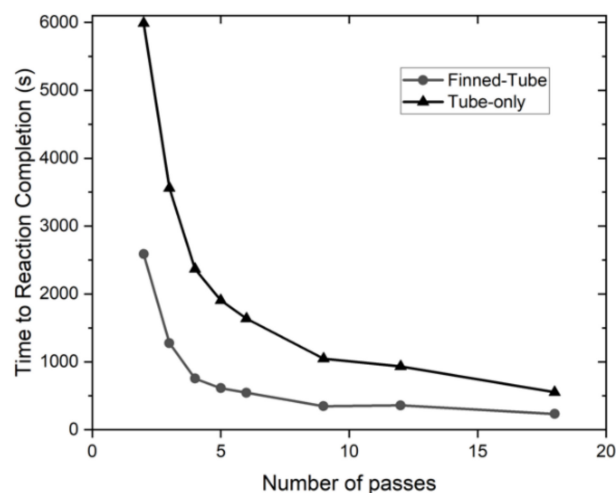

Figure 8. Time to reaction completion against the number of passes for tube-only and finned tube configurations.

From Figure 8, it is evident that a significant decrease in charging time is achieved by adding fins; this amounts to a 56% to 68% lower charging time compared to the tube-only configurations, shown in Figure 8. This brings the 6-, 9-, and 12-pass heat exchangers (finned tube configuration) to below 10 min charging time, with the 5-pass heat exchanger only 12.4 s above 10 min. The 9-pass configuration has a charge time of roughly 6 min, while the 18-pass configuration has a charge time of roughly 3.9 min. For an average consumer, 6 and 3.9 min are reasonable and comparable to the current gasoline filling times at commercial stations [31]. The current study has shown that more tubes with fins decrease the charge time due to the decreased distance between the hydride and the heat

exchanger. A further study on the pumping power is presented in the next section to find a complete optimum configuration.

5. Pumping Power Calculation

A high number of smaller tubes results in a shorter charge period and, consequently, an increased heat transfer rate. This significantly increases the pumping power for the R-134a flow. Methods for calculating the two-phase pumping power include the homogenous and separated flow models with the latter used frequently [32]. The most common separated flow model, namely, the Lockhart–Martinelli Correlation was adopted in this study [33]. An average R-134a quality of 0.6 was assumed for the analysis, thus eliminating complexities due to heating, volume expansion, and fluid property changes, while still allowing for adequate pressure drop calculation.

The required flow rate is dependent on the heat transfer rate of the heat exchanger. A constant flow rate, above the greatest required flow rate is used throughout the charging process. A MATLAB function was created using Equations (8)–(16) to solve for the pumping power [34].

Equation (8) describes the friction factor (f) as a function of Reynold's number, pipe roughness (ε) and inner pipe radius (r_1). The pipe roughness for aluminum tubes is 1×10^{-6} m.

$$f = \left(\frac{1}{-1.8 \log\left(\left(\frac{\varepsilon}{2r_1} \right)^{1.1} + \frac{6.9}{Re} \right)} \right)^2 \tag{8}$$

Using the friction factor, mass flux, inner pipe radius, and fluid density (ρ), the pressure gradient for each phase is found using Equation (9).

$$Liquid\ or\ Gas\ Pressure\ Gradient = \frac{f}{2}\left(\frac{G^2}{2\rho r_1} \right) \tag{9}$$

$$X = \sqrt{\left(\frac{liquid\ pressure\ gradient}{gas\ pressure\ gradient} \right)} \tag{10}$$

Equations (11) and (12) are used to find the pressure gradient multiplier (ψ), which depends on whether the fluid flow is laminar or turbulent. The total pressure gradients for each phase are equal and are found using Equation (13).

$$\psi_{Liquid} = \sqrt{1 + \frac{C}{X} + \frac{1}{X^2}} \tag{11}$$

$$\psi_{Gas} = \sqrt{1 + CX + X^2} \tag{12}$$

$$Total\ Pressure\ Gradient = \psi_{Liquid}^2 = \psi_{Gas}^2 \tag{13}$$

Once the pressure gradient for a major loss is found, Equation (14) is used to sum the pressure drop associated with features along the pipe (in this case, 180 degree turns). As the number of passes increases, the minor drop will increase accordingly due to the additional turns. The coefficient, K, can be found in any basic fluid mechanics literature [35].

$$Minor\ Pressure\ Loss = \sum K\left(\frac{G^2}{2\rho} \right) \tag{14}$$

Equation (15) calculates the total pressure drop along the coolant tube, as shown below.

$$\Delta P = Minor\ Pressure\ Loss + (Total\ Pressure\ Gradient \times Length) \tag{15}$$

Lastly, the pumping power is calculated using Equation (16) which is a function of mass flow rate ($\dot{m}$), specific volume of the fluid (v) at quality 0.6, and total pressure drop (ΔP).

$$Power \ = \ \dot{m}v\Delta P \qquad (16)$$

The input parameter is the maximum heat exchange rate (W/m) based on the volumetric heat generation minus heat capacity change of the hydride bed. For the required mass flow rate (kg/s) from the heat exchange, the process splits into two parts. The Lockhart–Martinelli Correlation uses a separated flow model, so the process is completed for both vapor and liquid phases. The mass flow rate of each phase is found using an average quality of 0.6, which is translated to mass flux, G (kg/m^{2}s).

Figure 9 displays the pump power (kW) and energy (kWh) as a function of number of passes. Presently, a system design optimization is required; there are pumps on the market that can fulfill all the requirements for each of the number of passes. For this study, the charge time and the pump requirements must be balanced to obtain the optimum configuration. From Figure 9, log-log plot, it is evident that the energy consumption (kWh) drastically increases between 9 and 12 passes and a significant jump between 6 and 9 passes. The energy requirement above 9 passes is unreasonably high for a hydrogen fueling application. Maintaining a lower energy requirement is beneficial for the cost and durability of the system components.
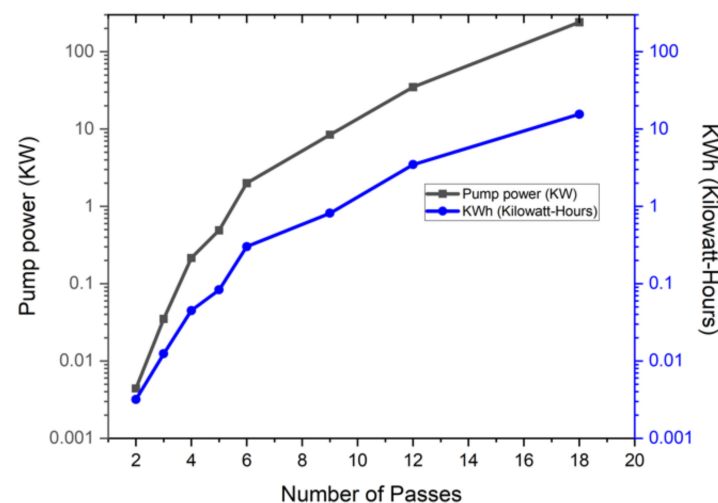

Figure 9. Pump flow requirements for finned tube configurations.

6. Conclusions

The performance of metal hydride reactors using Ti$_{1.1}$CrMn was studied under many different configurations. First, the area ratio of the heat exchange tubes to the reactor area was set to 0.1. Simulations were performed using COMSOL Multiphysics to determine the optimum spacing of the tubes; the number of tubes was varied from 2 to 18. Next, the simulations of longitudinal finned configurations were conducted to gauge the effect of fins on reactor performance.

1. An increased charging rate was observed in the finned tube configuration compared to the tube-only configurations due to the reduced average distance to the heat exchange tubes. Furthermore, the stagnated charging rate was observed at a higher average reacted fraction.

2. From Figure 8, it is evident that as the number of passes increases, the charge time decreases rapidly until the 5-pass heat exchanger; additionally, a further decrease in the charge time becomes less substantial with additional tubes.

3. A significant decrease in charging time was achieved by adding fins that amount to 56% to 68% lower charging time compared to the tube-only configurations; the results

show 6-, 9,- and 12-pass heat exchangers (finned tube configuration) to record less than 10 min of charging time. The 9-pass configuration has a charge time of roughly 6 min. Further, adding more tubes with fins decreases the charge time due to the reduced distance between the hydride and the heat exchanger.

4. From the pumping power calculations, the energy requirement above 9 passes were unreasonably high for a hydrogen fueling application. Maintaining a lower energy requirement is beneficial for the cost and durability of the system components.

Author Contributions: Conceptualization, M.D.K., V.K.K. and S.K.; methodology, M.D.K. and S.K.; software, M.D.K.; validation, M.D.K., V.K.K. and S.K.; formal analysis, M.D.K., V.K.K. and S.K.; data curation, M.D.K., V.K.K. and S.K.; writing—original draft preparation, M.D.K.; writing—review and editing, M.D.K., V.K.K. and S.K.; supervision, S.K. All authors have read and agreed to the published version of the manuscript.

Institutional Review Board Statement: Not applicable.

Informed Consent Statement: Not applicable.

Conflicts of Interest: The authors declare no conflict of interest.

Nomenclature

A	Area (m^2)
C	Pressure gradient multiplier coefficient
C_a	Hydriding constant (1/s)
c_p	Specific heat at constant pressure (J/kg-K)
D	Reactor diameter (m)
E_a	Activation energy for hydriding reaction (J/mol-H_2)
Ff	Fraction of reaction completionFriction factor
G	Mass flux (kg/m^2-s)
h	Heat transfer coefficient (W/m^2-K)
i	Index for heat transfer tubes
k	Thermal conductivity (W/m K)
K	Resistance Coefficient
L	Reactor length (m)
m	Mass (kg)
$\dot{m}$	Mass flow rate (kg/s)
MW	Molecular weight (g/mol)
n	Total for index of heat transfer tubes
P	Pressure (bar)
P_{eq}	Equilibrium pressure (Pa)
P_o	Atmospheric pressure (Pa)
$\dot{q}'''$	Heat generation rate (W/m^3)
R	Universal gas constant (J/mol-K)
Re	Reynold's number
r_1	Inner radius of heat exchange tube (m)
r_2	Outer radius of heat exchange tube (m)
T	Temperature (°C or K)
x, y, z	Coordinate axes
t	Time (s)
X	Lockhart–Martinelli factor
x	Longitudinal coordinate of tubes
$V_{HE\text{-}R}$	Volume ratio of heat exchanger to reactor volume
ΔH_r	Reaction enthalpy (J/mol-H_2)
ΔS	Reaction entropy (J/mol-H_2)

Greek symbols

ε	Pipe roughness (m)
ρ	Density (kg/m^3)
ν	Specific volume (m^3/kg)
φ	Porosity of metal hydride powder
ψ	Pressure gradient multiplier

Subscripts

Al	Aluminum
eff	Effective
H$_2$	Hydrogen
HE	Heat exchanger
i	Index for heat transfer tubes
MH	Metal hydride
R	Reactor

References

1. Pickering, L.; Lototskyy, M.V.; Davids, M.W.; Sita, C.; Linkov, V. Induction melted AB2-type metal hydrides for hydrogen storage and compression applications. *Mater. Today Proc.* **2018**, *5*, 10470–10478. [CrossRef]
2. Tarasov, B.P.; Fursikov, P.V.; Volodin, A.A.; Bocharnikov, M.S.; Shimkus, Y.Y.; Kashin, A.M.; Yartys, V.A.; Chidziva, S.; Pasupathi, S.; Lototskyy, M.V. Metal hydride hydrogen storage and compression systems for energy storage technologies. *Int. J. Hydrog. Energy* **2021**, *46*, 13647–13657. [CrossRef]
3. Abe, J.O.; APopoola, P.I.; Ajenifuja, E.; Popoola, O.M. Hydrogen energy, economy and storage: Review and recommendation. *Int. J. Hydrog. Energy* **2019**, *44*, 15072–15086. [CrossRef]
4. Office_of_Energy_Efficiency_ and _Renewable_Energy. *Hydrogen and Fuel Cell Technologies Office Multi-Year Research, Development, and Demonstration Plan*; Office of Energy Efficiency and Renewable Energy: Washington, DC, USA, 2014.
5. Muthukumar, P.; Singhal, A.; Bansal, G. Thermal modeling and performance analysis of industrial-scale metal hydride based hydrogen storage container. *Int. J. Hydrog. Energy* **2012**, *37*, 14351–14364. [CrossRef]
6. Nyamsi, S.N.; Yang, F.; Zhang, Z. An optimization study on the finned tube heat exchanger used in hydride hydrogen storage system–analytical method and numerical simulation. *Int. J. Hydrog. Energy* **2012**, *37*, 16078–16092. [CrossRef]
7. Garrison, S.L.; Hardy, B.J.; Gorbounov, M.B.; Tamburello, D.A.; Corgnale, C.; Mosher, D.A.; Anton, D.L. Optimization of internal heat exchangers for hydrogen storage tanks utilizing metal hydrides. *Int. J. Hydrog. Energy* **2012**, *37*, 2850–2861. [CrossRef]
8. Nam, J.; Ko, J.; Ju, H. Three-dimensional modeling and simulation of hydrogen absorption in metal hydride hydrogen storage vessels. *Appl. Energy* **2012**, *89*, 164–175. [CrossRef]
9. Bhouri, M.; Goyette, J.; Hardy, B.J.; Anton, D.L. Honeycomb metallic structure for improving heat exchange in hydrogen storage system. *Int. J. Hydrog. Energy* **2011**, *36*, 6723–6738. [CrossRef]
10. Dhaou, H.; Souahlia, A.; Mellouli, S.; Askri, F.; Jemni, A.; Nasrallah, S.B. Experimental study of a metal hydride vessel based on a finned spiral heat exchanger. *Int. J. Hydrog. Energy* **2010**, *35*, 1674–1680. [CrossRef]
11. Visaria, M.; Mudawar, I. Coiled-tube heat exchanger for high-pressure metal hydride hydrogen storage systems–Part 2. Computational model. *Int. J. Heat Mass Transf.* **2012**, *55*, 1796–1806. [CrossRef]
12. Visaria, M.; Mudawar, I. Coiled-tube heat exchanger for High-Pressure Metal Hydride hydrogen storage systems–Part 1. Experimental study. *Int. J. Heat Mass Transf.* **2012**, *55*, 1782–1795. [CrossRef]
13. COMSOL. *Multiphysics, Version 5.12016*; COMSOL: Stockholm, Sweden, 2015.
14. Jain, I.; Lal, C.; Jain, A. Hydrogen storage in Mg: A most promising material. *Int. J. Hydrog. Energy* **2010**, *35*, 5133–5144. [CrossRef]
15. Rusman, N.; Dahari, M. A review on the current progress of metal hydrides material for solid-state hydrogen storage applications. *Int. J. Hydrog. Energy* **2016**, *41*, 12108–12126. [CrossRef]
16. Sakintuna, B.; Lamari-Darkrim, F.; Hirscher, M. Metal hydride materials for solid hydrogen storage: A review. *Int. J. Hydrog. Energy* **2007**, *32*, 1121–1140. [CrossRef]
17. Jain, I.; Jain, P.; Jain, A. Novel hydrogen storage materials: A review of lightweight complex hydrides. *J. Alloy. Compd.* **2010**, *503*, 303–339. [CrossRef]
18. Flueckiger, S.; Voskuilen, T.; Pourpoint, T.; Fisher, T.S.; Zheng, Y. In situ characterization of metal hydride thermal transport properties. *Int. J. Hydrog. Energy* **2010**, *35*, 614–621. [CrossRef]
19. Pourpoint, T.L.; Velagapudi, V.; Mudawar, I.; Zheng, Y.; Fisher, T.S. Active cooling of a metal hydride system for hydrogen storage. *Int. J. Heat Mass Transf.* **2010**, *53*, 1326–1332. [CrossRef]
20. Visaria, M.; Mudawar, I.; Pourpoint, T.; Kumar, S. Study of heat transfer and kinetics parameters influencing the design of heat exchangers for hydrogen storage in high-pressure metal hydrides. *Int. J. Heat Mass Transf.* **2010**, *53*, 2229–2239. [CrossRef]
21. Voskuilen, T.; Zheng, Y.; Pourpoint, T. Development of a Sievert apparatus for characterization of high pressure hydrogen sorption materials. *Int. J. Hydrog. Energy* **2010**, *35*, 10387–10395. [CrossRef]
22. Voskuilen, T.G.; Pourpoint, T.L. Phase field modeling of hydrogen transport and reaction in metal hydrides. *Int. J. Hydrog. Energy* **2013**, *38*, 7363–7375. [CrossRef]

23. Liu, Y.; Li, H.-W.; Huang, Z. Editorial: Metal Hydride-Based Energy Storage and Conversion Materials. *Front. Chem.* **2020**, *8*, 675. [CrossRef] [PubMed]

24. Dalkilic, A.; Celen, A.; Çebi, A.; Wongwises, S. Empirical correlations for the determination of R134a's convective heat transfer coefficient in horizontal and vertical evaporators having smooth and corrugated tubes. *Int. Commun. Heat Mass Transf.* **2016**, *76*, 85–97. [CrossRef]

25. Fang, X. A new correlation of flow boiling heat transfer coefficients based on R134a data. *Int. J. Heat Mass Transf.* **2013**, *66*, 279–283. [CrossRef]

26. Grauso, S.; Mastrullo, R.; Mauro, A.; Thome, J.; Vanoli, G.P. Flow pattern map, heat transfer and pressure drops during evaporation of R-1234ze (E) and R134a in a horizontal, circular smooth tube: Experiments and assessment of predictive methods. *Int. J. Refrig.* **2013**, *36*, 478–491. [CrossRef]

27. Kaew-On, J.; Wongwises, S. New proposed two-phase multiplier and evaporation heat transfer coefficient correlations for R134a flowing at low mass flux in a multiport minichannel. *Int. Commun. Heat Mass Transf.* **2012**, *39*, 853–860. [CrossRef]

28. Kundu, A.; Kumar, R.; Gupta, A. Heat transfer characteristics and flow pattern during two-phase flow boiling of R134a and R407C in a horizontal smooth tube. *Exp. Therm. Fluid Sci.* **2014**, *57*, 344–352. [CrossRef]

29. Suda, S.; Kobayashi, N.; Yoshida, K. Reaction kinetics of metal hydrides and their mixtures. *J. Less Common Met.* **1980**, *73*, 119–126. [CrossRef]

30. Visaria, M.; Mudawar, I.; Pourpoint, T. Enhanced heat exchanger design for hydrogen storage using high-pressure metal hydride: Part 1. Design methodology and computational results. *Int. J. Heat Mass Transf.* **2011**, *54*, 413–423. [CrossRef]

31. Wang, Y.-W.; Lin, C.-C. Locating road-vehicle refueling stations. *Transp. Res. Part E: Logist. Transp. Rev.* **2009**, *45*, 821–829. [CrossRef]

32. Singal, L.; Sham, R.; Kumar, S. Single and two phase pressure drop in fluid flow: A review. *Int. J. Latest Trends Eng. Technol.* **2015**, *6*, 28–33.

33. Lockhart, R.W. Proposed correlation of data for isothermal two-phase, two-component flow in pipes. *Chem. Eng. Prog.* **1949**, *45*, 39–48.

34. *MATLAB*; Version R2016b; MathWorks: Natick, MA, USA, 2016.

35. Santos-Ruiz, I.; López-Estrada, F.-R.; Puig, V.; Valencia-Palomo, G. Simultaneous Optimal Estimation of Roughness and Minor Loss Coefficients in a Pipeline. *Math. Comput. Appl.* **2020**, *25*, 56. [CrossRef]